PNAS
www.pnas.org

Main Manuscript for

A new sea-level record for the Neogene/Quaternary boundary reveals transition to a more stable East Antarctic Ice Sheet.

Kim A. Jakob[1*], Paul A. Wilson[2], Jörg Pross[1], Thomas H. G. Ezard[2], Jens Fiebig[3], Janne Repschläger[4], Oliver Friedrich[1]

[1]Institute of Earth Sciences, Heidelberg University, Im Neuenheimer Feld 234–236, 69120 Heidelberg, Germany.

[2]University of Southampton, National Oceanography Centre Southampton, European Way, Southampton SO14 3ZH, UK.

[3]Institute of Geosciences, Goethe-University Frankfurt, Altenhöferallee 1, 60438 Frankfurt, Germany.

[4]Climate Geochemistry Department, Max Planck Institute for Chemistry, Hahn Meitner Weg 1, 55128 Mainz, Germany.

*To whom correspondence should be addressed. **E-Mail**: kim.jakob@geow.uni-heidelberg.de

Classification

Physical Sciences (Earth, Atmospheric and Planetary Science)

Keywords

East Antarctic Ice Sheet, sea level, ocean-cryosphere interaction, intensification of Northern Hemisphere Glaciation

Abstract

Sea-level rise resulting from the instability of polar continental ice sheets represents a major socio-economic hazard arising from anthropogenic warming, but the response of the largest component of Earth's cryosphere, the East Antarctic Ice Sheet (EAIS), to global warming is poorly understood. Here we present a detailed new record of North Atlantic deep-ocean temperature, global sea-level and ice-volume change for ~2.75–2.4 million years (Ma) ago, when atmospheric carbon dioxide concentrations (pCO_2) ranged from present-day (>400 parts per million volume, ppmv) to pre-industrial (<280 ppmv) values. Our data reveal clear glacial-interglacial cycles in global ice volume and sea level largely driven by the growth and decay of ice sheets in the Northern Hemisphere. Yet sea-level values during Marine Isotope Stage (MIS) 101 (~2.55 Ma) also signal substantial melting of the EAIS, and peak sea levels during MIS G7 (~2.75 Ma) and, perhaps, MIS G1 (~2.63 Ma) are also suggestive of EAIS instability. During the succeeding glacial-interglacial cycles (MIS 100–95), sea levels were distinctly lower than before, strongly suggesting a link between greater stability of the EAIS and increased land-ice volumes in the Northern Hemisphere. We propose that lower sea levels driven by ice-sheet growth in the Northern Hemisphere decreased EAIS susceptibility to ocean melting. Our findings have implications for future EAIS vulnerability to a rapidly warming world.

Significance Statement

We studied the response of global ice volume/sea level to climate forcing ~2.75–2.4 million years ago (Ma), when atmospheric CO_2 levels last lay in a range similar to the last two centuries. Our data reveal clear cycles in global sea level largely driven by the growth/decay of Northern Hemisphere ice sheets. Peak sea levels suggest melting of East-Antarctic land-ice prior to ~2.53 Ma. Thereafter, glacial and interglacial sea levels are distinctly lower than before, suggesting that the growth of larger Northern Hemisphere ice sheets lowered sea level globally and acted to stabilize the East Antarctic Ice Sheet by limiting its exposure to warm ocean-waters. Our findings provide a framework to help understand ice-volume variability under warmer-than-pre-industrial climates.

Main text

Introduction

The instability of polar continental ice sheets in a warmer future is an issue of major societal concern (1-5). Based on linear extrapolation of recent sea-level rise (2), mean global sea level could increase by 65 ± 12 cm by 2100 relative to the 2005 baseline, consistent with Intergovernmental Panel on Climate Change projections (1) of a ~30–100 cm increase by 2100. Further, satellite observations (4) document substantial mass loss of both the Greenland Ice Sheet (GIS) and the West Antarctic Ice Sheet (WAIS) over the past decade – the two ice sheets that are most susceptible to global warming because of rapidly rising Arctic air temperatures (1) (GIS) and vulnerability to ocean-atmospheric warming (5, 6) (WAIS). The mass balance of the much larger EAIS and its contribution to ongoing sea-level change, however, remain poorly constrained (1).

The role of pCO_2 as a driver of long-term changes in ice-volume and sea-level over the Cenozoic era (past ~66 million years (Myr)) is widely documented (7-9) and there is compelling evidence (6, 10-12) of EAIS retreat during warm intervals of the Pliocene epoch between ~5.3 and 3.3 Ma when pCO_2 levels (13, 14) last reached values close to the present-day (~400 ppmv; Fig. 1a–b; see *SI Appendix, Section 1*). But there is disagreement over EAIS behavior under pCO_2 levels (13) similar to those of pre-industrial Quaternary times (<280 ppmv). A compilation of marine geochemical palaeo-sea-level and pCO_2 records suggests that the EAIS was stable under these conditions (7). In contrast, while the amplitudes of change are controversial (15) (see *SI Appendix, Section 2*), sea-level reconstructions from paleoshorelines (16) and benthic geochemical data (9, 17, 18) (Fig. 2) imply EAIS melting during the

Quaternary "super-interglacials" of MIS 11 (~400 thousand years ago [ka]) and 31 (~1.07 Ma) under relatively low pCO_2 conditions. Supporting evidence for EAIS retreat during the most recent "super-interglacial" MIS 11 comes from isotope measurements in mineral deposits recording past changes in subglacial East Antarctic waters (19), as well as records of ice-rafted debris (IRD) and detrital sediment neodymium isotopes from offshore the Wilkes Subglacial Basin (20). The latter records (20) also indicate EAIS retreat during the last interglacial MIS 5e (~120 ka). Melting of the EAIS as inferred in the late Quaternary was likely driven by ocean-atmosphere warming around Antarctica and grounding-line retreat in response to ice-ocean interactions (19, 20).

To further investigate past EAIS response to climate forcing we studied the Neogene/Quaternary transition when mean pCO_2 (13, 21) fell from levels similar to the anthropogenically perturbed values of today into the Quaternary range, leading to progressive high-latitude cooling and the intensification of Northern Hemisphere Glaciation (22-26) (iNHG; Fig. 1a–b). Our approach is based on a simple approximation that, once estimated past global sea level exceeds 11.6 meters sea-level equivalent (msle) above modern, which corresponds to the complete melting of the present-day GIS (7.3 msle (27, 28)) and the marine- and land-based WAIS (3.4 and 0.9 msle (28, 29), respectively), EAIS instability (i.e., a retreat from its present-day size) can be inferred (see *SI Appendix, Section S4.1* for details). We quantified sea-level and ice-volume changes for the interval ~2.75 to 2.4 Ma (MIS G7–95) by measuring the oxygen-isotope composition ($\delta^{18}O$) and Mg/Ca ratio in well-preserved benthic foraminiferal calcite (*Oridorsalis umbonatus*) from Integrated Ocean Drilling Program (IODP) Site U1313 (41°0'N, 32°57'W; 3426 m water depth (30)) in the North Atlantic Ocean (Fig. 1c–d). Using this approach we reconstructed changes in seawater $\delta^{18}O$ ($\delta^{18}O_{sw}$), a proxy for global sea level and continental ice volume (31). This was done by (i) calculating bottom-water temperatures (BWT) derived from Mg/Ca (32) (Fig. 1e), (ii) combining Mg/Ca-derived BWTs with $\delta^{18}O$ to determine $\delta^{18}O_{sw}$ (33) (Fig. 1f), and (iii) converting $\delta^{18}O_{sw}$ to sea level using a relationship between changes in sea level and $\delta^{18}O_{sw}$ of 0.011 ‰m^{-1} (34) (see *Methods*; Fig. 1f). 95 % probability intervals calculated through Monte Carlo Simulations for individual sea-level data points yield an average uncertainty for our sea-level estimates of ± 28 m (~2σ (SD)) (see *Methods*; Fig. 1f), roughly equivalent to the decay/growth of ice four times greater than the GIS. Our approach was validated by reconstructing $\delta^{18}O_{sw}$ for the Recent (~0–7 ka) at IODP Site U1313 and for late Holocene core-top (multicorer) samples from a neighbouring site (MSM 58) which are indistinguishable from the observed modern-day values (see *Methods* and *SI Appendix, Section S4.2.8* for details).

Underlying assumptions of sea-level reconstruction

We have minimized the aliasing effects on our records of post-depositional diagenetic alteration and sampling by using exceptionally well-preserved, uncontaminated foraminiferal calcite (see *SI Appendix, Sections S4.2.1* and *S4.2.2*) and our $\delta^{18}O$ and Mg/Ca records are true pairs, generated on aliquots of pooled specimens. Nevertheless, there are other sources of uncertainty to consider (see the review of ref. (35) and references therein). Ocean *pH* and the $\delta^{18}O$ and Mg/Ca composition of the parent water at our study site ($\delta^{18}O_{sw}$ and Mg/Ca_{sw}), as well as the Mg/Ca-BWT calibration and the sea-level-$\delta^{18}O_{sw}$ conversion applied all have the potential to influence the BWT and sea level record. Calculated absolute temperatures and sea levels are necessarily more uncertain than amplitudes of relative change, but we designed our study to minimize these uncertainties and to take a conservative approach to estimate sea-level maxima and ice-sheet retreat during interglacials (hereafter sl-con_{IGs}).

Our study interval is short in comparison to the oceanic residence time of Mg so we can rule out large fluctuations of Mg/Ca_{sw}. However, the absolute Mg/Ca_{sw} value across the Neogene/Quaternary boundary was probably different to today (5.2 mol/mol) (36). Our calculations follow reference (36) by employing a steady increase in Mg/Ca_{sw} across our study interval from 4.25 to 4.4 mol/mol, and we selected a benthic foraminifer that shows low sensitivity in its Mg-partitioning behavior to changes in Mg/Ca_{sw} (31). Our sensitivity tests (see *SI Appendix, Section S4.2.6*) show that a Mg/Ca_{sw} ratio lower than 1.9 to 3.7 mol/mol is required to contradict our main conclusions – an unrealistically large deviation from both the modern value and published estimates for the Neogene/Quaternary transition (36). Furthermore, the shallow infaunal habitat of *O. umbonatus* (31) means that, in rapidly accumulating $CaCO_3$-rich sediments such as those at Site U1313, this species is well buffered from the impact of changes in ocean *pH* on Mg-partitioning (see *SI Appendix, Section S4.2.7*).

Two sources of uncertainty with respect to $\delta^{18}O_{sw}$ must be considered for our sea-level calculations. First, the global value for $\delta^{18}O_{sw}$ is related to global land-ice volume, but $\delta^{18}O_{sw}$ shows spatial variability even in the deep oceans; we therefore allow for the influence of incursions of Antarctic Bottom Waters into the deep North Atlantic during glacials (37) by normalizing Antarctic Bottom Water and North Atlantic Deep Water following ref. (38) (see *Methods* and *SI Appendix, Section S4.2.4*). Second, temporal change in the $\delta^{18}O$ composition of accumulating or melting ice can influence the relationship between $\delta^{18}O_{sw}$ and calculated sea level through time (11, 28, 35). Therefore, the selection of an appropriate sea-level-$\delta^{18}O_{sw}$ conversion factor is critical because variability in the $\delta^{18}O$ composition of glacial ice within and among ice sheets means that calculations are potentially sensitive to the locus of growth/melt. Sea-level-$\delta^{18}O_{sw}$ conversion factors ranging between 0.008 and 0.014 ‰m^{-1} have been suggested (11, 34, 39, 40) (Fig. 2). Conversion factors between 0.008 and 0.011 ‰m^{-1} are inferred (34, 39-41) for ice-volume changes predominantly occurring in the high northern latitudes. For Antarctica (11) a conversion factor of 0.014 ‰m^{-1} is typically assumed, but when ice melt derives from marine-grounded sectors, the sea-level-$\delta^{18}O_{sw}$ relation deviates from linearity (Fig. 2). "Best sea-level estimates" for our study (sl-con_{IGs}; Tab. 1) are calculated using the 0.011 ‰m^{-1} conversion factor (34) (see *SI Appendix, Section S4.2.3*). Using this conversion factor is a conservative approach, because it yields lower amplitudes of glacial-interglacial sea-level change than the 0.008–0.010 ‰m^{-1} sea-level-$\delta^{18}O_{sw}$ conversions (39, 40)

(Fig. 2). To test the robustness of our main conclusions we also calculated "most conservative estimates" applying the non-linear sea-level-$\delta^{18}O_{sw}$ relation (11) (Tab. 1) that further minimizes both absolute sea levels and amplitudes of change (see *Methods*). In the following, reported sea-level values are best estimates (sl-con_{IGs}) unless otherwise stated.

Results and Discussion

Increasing amplitudes of sea-level change with iNHG

Our record of sea-level change ranges between ~44 ± 28 m above modern during interglacial MIS 101 and ~135 ± 28 m below modern during glacial MIS 96 (Fig. 1f). It reveals clear glacial-interglacial cycles from MIS G7 through 95, with lower amplitudes before MIS 100 (~2.53 Ma) (typically ~50–90 m) and larger amplitudes from MIS 100 onward (typically ~80–120 m) driven largely by a ~40 m lowering of sea-level minima from, on average, ~60 ± 28 m below modern (prior to MIS 100) to ~100 ± 28 m below modern (from MIS 100 onward). Sea levels are not only distinctly lower during MIS 100, 98 and 96 than in the older glacials in our record, but they are also lower for the intervening interglacials (MIS 99, 97 and 95) than for the older peak interglacials (Fig. 1f). We attribute this pattern to the growth of more land ice in the Northern Hemisphere during glacials MIS 100 through 96 and its partial survival into intervening interglacials. For the studied time interval, knowledge of interglacial ice masses is extremely limited, but a synthesis of empirical data and numerical modeling results for late Pleistocene ice sheets (42) suggests that the GIS, probably with some minor contributions from the Laurentide Ice Sheet (LIS), are the most likely candidates for this behavior.

Our finding of enhanced amplitudes of glacial-interglacial change and a lowering of glacial sea-levels from MIS 100 through 96 is consistent with evidence from both terrestrial (occurrence of Missouri tills (24)) and marine (IRD in the North Atlantic (22, 23, 43)) geological records (Fig. 3a–c). These studies, together with global ice-volume simulations (44), suggest major glaciation of Greenland (GIS), Scandinavia (Scandinavian Ice Sheet) and North

America (LIS) during MIS 100, 98 and 96 (43). Proxy data further indicate that MIS 100 was the first glacial of the iNHG during which the LIS advanced into the mid-latitudes (24) and large-scale ice rafting occurred across the North Atlantic Ocean to the southern fringes of the Last Glacial Maximum IRD belt (22, 23, 43). Terrestrial climate records from Lake El'gygytgyn in northeastern Russia (45) complement this general picture (Fig. 3d). Pollen spectra indicate that summer temperatures in the high northern latitudes cooled substantially during MIS 100, approaching values similar to those of late Pleistocene glacials (46). Furthermore, the occurrence of lacustrine facies consistent with perennial ice cover during glacial times in Lake El'gygytgyn (46) (Fig. 3b) documents two additional glacial advances of Northern Hemisphere ice sheets following MIS 100 at ~2.49 Ma (MIS 98) and ~2.44 Ma (MIS 96) when our record signals sea-level lowstands that are even more pronounced than for MIS 100 (Fig. 3a).

The only other high-resolution sea-level record for our study interval comes from the Mediterranean Sea (47) and is based on a different methodology than the one used herein and elsewhere (9, 18, 44, 48, 49). It suggests glacial lowstands during MIS 100, 98 and 96 that are barely below modern sea level and proposes a ~0.6 Ma-long decoupling between deep-sea cooling at ~2.73 Ma and major glaciation at ~2.15 Ma. Those interpretations are untenable based on our new record and previously available reconstructions (9, 18, 44, 48). Our record documents prominent sea-level lowstands from at least MIS G6 onward that are more in keeping with the chronology of iNHG developed from extensive marine (22, 23) and terrestrial (24) records (Fig. 3a–d).

Other published sea-level records (9, 18, 35, 44, 47-50) covering the iNHG are typically of low temporal resolution and partly contradictory. Our record shows a well-defined glacial-interglacial structure with typically higher-amplitude changes than those other records largely because our data signal more pronounced sea-level fall during glacials, particularly from MIS 100 though 96 (Fig. 4a–b; see also *SI Appendix, Section S5.1*). One main factor responsible for larger amplitude changes in our record relative to others is the tendency for more highly resolved datasets to better capture more of the glacial-interglacial signal. More highly resolved datasets are needed to verify the full influence of this effect, but our analysis suggests it explained ~20 % of the variation in the amplitude of benthic $\delta^{18}O$ (and thus sea-level) records across MIS 101 through 100 before our study, and ~30 % including our new record (Fig. 4c). A second factor contributing to the lower sea levels that we construct arises as a side-effect of calculating sea levels using a method that prioritizes conservative estimation of interglacial sea-level maxima, i.e., ice-sheet retreat (sl-con$_{IGs,}$ see *Methods* for details). Adapting our calculations to instead prioritise conservative estimation of glacial sea-level minima, i.e., ice-sheet growth (sl-con$_{Gs}$; see *SI Appendix, Section S5.2* for details) yields less extreme, mean sea-level values of ~70 m below modern for MIS 100 (Fig. 4b). This value is closer to – but still nearly 20 % lower than – the lowest of the previous sea-level estimates from less well resolved datasets (Fig. 4b) and implies a correspondingly greater land-ice budget despite the low-slung profile of early northern ice sheets (51, 52) (see also *SI Appendix, Section S5.3*). Regardless, our main findings are unchanged: sea levels are distinctly lower than before both during glacials (MIS 100, 98 and 96) and during the intervening interglacials (MIS 99 and 97).

EAIS instability

Some model-derived sea-level estimates (48) suggest that highstands did not exceed 11.6 msle above modern for the past ~5.3 Myr, implying maintenance during interglacials of an EAIS at least as large as today. That suggestion, however, is not readily reconciled with other model-based (6) and sedimentological (10) evidence documenting a dynamic behavior of the EAIS during the early Pliocene. Some proxy-based records (9, 18, 47, 49, 50) also yield sea levels >11.6 msle for some interglacials in our study interval (Fig. 4a), but their validity has been called into question (see *SI Appendix, Sections S3* and *S5.1* and references therein). In contrast, even our most conservative calculations indicate peak sea-level highstands that exceed the 11.6

msle threshold clearly during interglacials MIS 101 and, for at least some portion of MIS G7 (22 and 20 ± 28 m above modern, respectively), and our best estimates also point to a temporarily smaller EAIS than today during interglacial MIS G1 (18 ± 28 m above modern; Tab. 1, Fig. 2). These calculated sea-level highstands imply a retreat of all marine-based sectors of the EAIS, which presently store ice equivalent to ~19 msle (29). This observation is broadly consistent with (i) 3D ice-sheet model results (53) showing that a retreat of almost all marine-based ice of the EAIS is plausible under $p\mathrm{CO_2}$ conditions of 400 ppmv and (ii) geological evidence (19, 20) for substantial ice-margin retreat of the EAIS during late Quaternary interglacials MIS 11, 9 and 5. Our record of sea-level and inferred ice-volume changes suggests a dynamic response of the EAIS to interglacial radiative forcing across MIS 101 (~2.55 Ma) and, perhaps, even earlier to at least ~2.75 Ma (MIS G7) under conditions of modest $p\mathrm{CO_2}$ levels (Fig. 1b, f), and this conclusion is robust even for our most conservative reconstruction of ice-volume/sea-level variability (Tab. 1, Fig. 2; see also *SI Appendix, Section S4.2*). From ~2.53 Ma onward, however, sea-level highstands were consistently lower, falling well below the 11.6 msle threshold value – a pattern that is clear in both our most conservative and our best interglacial (sl-con$_{\mathrm{IGs}}$) estimates (Fig. 1e, 2) – and thus signaling a larger, more stable EAIS. The structure of the benthic oxygen isotope composite suggests that this stability endured for most of the Quaternary until the super-interglacials of the late Pleistocene, e.g., MIS 11 and 5 (Fig. 1a), for which retreat has already been proposed based on independent lines of evidence (19, 20) (Fig. 2).

EAIS dynamics controlled by ocean-cryosphere interactions

Orbitally paced insolation forcing and changing $p\mathrm{CO_2}$ play a prominent role in controlling late Pleistocene global ice-volume variations (7, 8). However, the combined influence of these two forcing factors do not offer a straightforward explanation for the inferred retreat of the EAIS during interglacial MIS 101 and the short-term destabilization during interglacials MIS G7 and, perhaps, G1 (see *SI Appendix, Section S6.1*). Southern Hemisphere insolation (54) was not unusually high during these interglacials compared to other interglacials in our study interval (Fig. 3f) and published records, albeit of modest temporal resolution, suggest that pCO_2 levels for MIS 99 and 97 are similar to or even exceed those of MIS 101 (21) (Fig. 1b). Thus, the influence of at least one other pivotal factor in addition to top-down radiative forcing is needed to explain inferred interglacial retreat of the EAIS. A potential mechanism to consider is sub-surface melting in response to ocean warming because it controls the volume of the Antarctic Ice Sheet today (55). Higher mean sea levels than today due to ice melt in the Northern Hemisphere increases the likelihood of Antarctic Ice Sheet exposure to the direct influence of warm ocean waters melting marine-grounded sectors of the ice sheet – ice shelves – from below. Removal of ice shelves reduces backstress and enhances seaward ice flow, thereby further enhancing ice melt and sea-level rise, and potentially pushing the Antarctic Ice Sheet toward a runaway marine ice-sheet instability (56). This mechanism may be particularly significant for the WAIS and marine-terminated EAIS basins with reverse-sloping beds that deepen towards the ice-sheet center (e.g., the Recovery Basin) (6, 57).

Links between EAIS ice-sheet stability, orbital forcing, pCO_2, high-latitude (ocean) temperature and Southern Ocean sea-ice extent are widely invoked (12, 19, 20, 58). As elaborated upon in the following, we here propose an ocean-cryosphere interaction in which glacial ice storage in the Northern Hemisphere had a positive feedback effect on global ice volume during the culmination of iNHG through sea-level-led EAIS stabilization.

Reduced marine basal melt increased EAIS stability

Starting with MIS 100 in our record, sea-level lowstands are distinctly lower than before even for our most conservative glacial estimates (sl-con$_{Gs}$; see *SI Appendix, Section S5.2* for details) – a pattern consistent with sea-level reconstructions derived from previous work (9, 18) (Fig. 4a). Both proxy records (22, 24) (Fig. 3b–d) and simulations of global ice-volume changes (44) indicate that this sea-level lowering was predominantly driven by increased ice growth in the Northern Hemisphere. The latter was associated with a decrease in astronomically driven peaks in solar radiation (54) (Fig. 3e), but ultimately caused by increased CO_2 sequestration in the deep Atlantic during cold stages (59), which was initiated by a fundamental reorganization of glacial deep-ocean circulation and reduced ocean-atmosphere exchange processes from the late Pliocene onward (49, 58). This reorganization was in turn driven by surface-water cooling in the high southern latitudes together with the expansion of Antarctic Ice Sheets (49, 58) (see *SI Appendix, Section S6.1*). Glacials from MIS 100 onward in our reconstruction also terminate to produce highstands (~8 ± 28 m above, and ~6 and ~11 ± 28 m below modern for MIS 99, 97, and 95, respectively) that are distinctly lower than the one reached during MIS 101 (~44 ± 28 m above modern; Fig. 3a), roughly approaching today's level. We hypothesize that residual land ice grown on the continents of the Northern Hemisphere during major glacials (MIS 100, 98 and 96), possibly the GIS and the LIS (42), survived into subsequent interglacials (MIS 99–95). This ice storage suppressed interglacial sea levels, protecting the EAIS from exposure to marine basal melting of ice shelves and promoting stability of the EAIS.

Our hypothesis for a decreasing marine influence and thus a more stable EAIS from ~2.53 Ma onward gains support from simulations of global ice-volume changes (44), suggesting that ice in the Northern Hemisphere equivalent to ~10 msle survived into interglacials MIS 99–95 (see *SI Appendix, Section S6.2*). Supporting evidence for increased stability of the EAIS from ~2.53 Ma comes from two lines of evidence in geological records from circum-Antarctica. First, there is a significant decrease in the accumulation of IRD in the Wilkes Subglacial Basin at ~2.5 Ma (12) (Fig. 3g). The second line of evidence (60) comes from sediment drifts off Prydz Bay, East Antarctica, documenting a decrease in sedimentation rates and a lack of IRDs signaling stabilization of the Lambert Glacier system – the largest ice stream on East Antarctica – at ~2.5 Ma. Simulations of surface-air temperature anomalies over Antarctica (44) suggest that the observed stabilization of the EAIS is unrelated to melting driven by the atmosphere. Thus, we propose that sea level-led changes in basal melting strongly influenced EAIS (in)stability alongside pCO_2 change and orbital forcing during the studied interval (see *SI Appendix, Section S6.1*).

Our records strongly suggest a dynamic behaviour of the EAIS prior to ~2.53 Ma, with retreat during interglacial MIS 101 most clearly indicated. Lower sea levels in our record following the culmination of the iNHG suggest that the development of major ice sheets in the north at ~2.53 Ma played a decisive role in EAIS stabilization through lowered glacioeustatic sea levels and reduced basal marine melting. Our detailed records provide a framework to help understand ice-volume variability in a bipolar-glaciated world under pCO_2 conditions similar to those of today and the near future.

Figure legends

Figure 1. Neogene to Quaternary climate and sea-level evolution. a, LR04 stack (25) for the past 5 Myr; arrow indicates the iNHG (~3.6–2.4 Ma) and its culmination (thick-arrowed interval) (61); green line indicates the benthic $\delta^{18}O$ level associated with MIS 101. **b,** Atmospheric pCO_2 estimates of refs. (13) (blue) and (21) (purple) for the past 5 Myr; the late Quaternary glacial-interglacial pCO_2 range (1) is indicated as pre-industrial pCO_2 band. Yellow shading in **a** and **b** highlights study interval (~2.75–2.4 Ma; c–f). **c, d,** Site U1313 benthic $\delta^{18}O$ and Mg/Ca raw data, respectively. **e,** Site U1313 deep-sea temperature. **f,** Site U1313 $\delta^{18}O_{sw}$-based sea level relative to present (black line); blue shading: 95 % probability interval from Monte Carlo Simulations (2σ); red line: threshold (11.6 msle) above which a smaller-than-present EAIS is signaled (27-29); m = marine part of EAIS, t = terrestrial part of EAIS. Glacials highlighted in grey.

Figure 2. Implication of different sea-level-$\delta^{18}O_{sw}$ conversions for estimates of interglacial ice-volume loss. Y-axis shows lower-than-modern $\delta^{18}O_{sw}$ values ($\Delta\delta^{18}O_{sw}$) and the x-axis (log-

scale) the corresponding sea-level increase for commonly used conversion factors (34, 39, 40) (0.011 [black], 0.010 [purple], 0.008 ‰m^{-1} [red]) and those for Antarctica only (11) (0.014 ‰m^{-1}) ignoring (yellow) and incorporating (brown) the impact of its marine-based ice sheets. Stars mark $\Delta\delta^{18}O_{sw}$ for interglacials of this study and corresponding sea-level equivalents in dependence of the conversion applied. Orange, blue and purple diamonds show the same for MIS 31, 11 (18), and 5e (17), respectively. Vertical lines indicate the sea-level increase resulting from complete melting of the GIS (+ 7.3 m), WAIS (+ 4.3 m), and EAIS (+ 53.3 m) (27-29).

Figure 3. Neogene to Quaternary marine and terrestrial climate proxy records. a, Sea-level (this study) relative to present (black line); red line: threshold (11.6 msle) above which a smaller EAIS than today is signaled (27-29); m = marine part of EAIS, t = terrestrial part of EAIS. **b,** Age of lacustrine sediments consistent with perennial ice cover during glacial times at Lake El'gygytgyn (46) (pink) and Missouri tills (24) (width reflects 1σ uncertainty; purple). **c,** IRD from Site U1313 (22, 23), southerly limit of the North Atlantic IRD belt. **d,** Mean temperature of the warmest month at Lake El'gygytgyn based on pollen spectra (45). **e,** Mean summer insolation at 65 °N (54); dashed lines indicate average peak (maximum) insolation values**. f,** Mean summer insolation at 65 °S (54). **g,** IRD from Site U1361 (12) offshore the Wilkes Subglacial Basin, Antarctica Glacials highlighted in grey.

Figure 4. Compilation of selected Neogene to Quaternary sea-level records. Sea-level estimates relative to present (black line) for the **a,** ~2.75–2.4 Ma (MIS G7–95) interval and **b,** ~2.55–2.50 Ma (MIS 100) interval; red line: threshold (11.6 msle) above which a smaller EAIS than today is signaled (27-29); m = marine part of EAIS, t = terrestrial part of EAIS. Sea-level values of this study in blue (solid line: best estimate approach ensuring sea levels for interglacials are calculated conservatively (sl-con_{IGs}; see Section *Palaeotemperature and sea-*

level reconstructions of the *Methods* for details); dashed line: adapted approach ensuring more conservative glacial values (sl-con$_{Gs}$)), of ref. (9) in grey, of ref. (44) in purple, of ref. (47) in brown, of ref. (18) in blue-green, and of ref. (48) in black. **c,** Relation between sample spacing and amplitude in benthic $\delta^{18}O$ records for MIS 100 and 101 (for references see *SI Appendix, Supplementary Table 3 for details*): As sampling resolution increases, the amplitude of the recovered signal increases (coef. = -0.16261, s.e. = 0.04559, $p < 0.01$) with no detectable difference between MIS 101 and MIS 100 (coef. = 0.11128, s.e. = 0.06448, $p > 0.05$), which explains 30.4 % of data variability.

Table 1. Comparison of our best *vs.* most conservative interglacial sea-level estimates for which we propose a smaller EAIS than today.

Materials and Methods

Sample material and processing

A total of 340 samples from IODP Site U1313 (41°0’N, 32°57’W, 3426 m water depth (30)) were used, taken along the primary shipboard splice from 131.06 to 114.12 meters composite depth (mcd), covering the interval from 2.76 to 2.41 Ma (MIS G7–95) following the age model of ref. (22). Our baseline resolution was achieved using samples with an 8-cm spacing (temporal resolution of ~1500 yr), but measurements were undertaken at higher resolution across glacial terminations (4-cm spacing, ~750 yr), interglacials MIS G7, G1 and 101 (4-cm to 2-cm spacing, ~750–375 yr) and glacial MIS 100 (2-cm spacing, ~375 yr). In addition, 7 samples from the uppermost section of IODP Site U1313 (“most recent samples”; 0–0.25 mcd, corresponding to ~0–7 ka (62)) and 9 core-top samples (~33°5’N–41°2‘N, 28°1’W–36°1’W, ~2600–3500 m water depth) from R/V Maria S. Merian cruise MSM58 (63) were investigated to ensure the overall validity of our approach, as benthic carbonate extracted from these samples is expected to reflect modern deep-water conditions (see *SI Appendix, Section S4.2*). These samples were processed with exactly the same methodology (as outlined below) applied to the MIS G7–95 samples from IODP Site U1313 (best sea-level estimates (sl-con_{IGs})) unless stated otherwise.

An average of twelve specimens of the benthic foraminifer *Oridorsalis umbonatus* was picked from the >150 μm dried sediment fraction of each sample. For combined $\delta^{18}O$ and Mg/Ca analysis, tests were cracked open and two splits were taken from this single pool of individuals (~1/3 of the pool was used for $\delta^{18}O$ and ~2/3 for Mg/Ca analysis). We selected the species *O. umbonatus* for our study for four reasons. First, it is buffered to the influence of changes in seawater carbonate ions (64) (i.e., deep ocean *pH*). Second, it shows a low sensitivity to temporal variations in Mg/Ca_{sw} (31). Third, its large chambers are easier to clean for Mg/Ca analysis than other taxa, and fourth, it is consistently present throughout the studied core sections.

Foraminiferal preservation

The preservation of *O. umbonatus* tests in our samples was examined by Scanning Electron Microscope (SEM) and Binocular Microscope. We studied representative specimens from both glacial and interglacial intervals. Close-up views were generated using a ZEISS SIGMA SEM at the Institute of Geosciences, Goethe-University Frankfurt, Germany, and a ZEISS SteREO Discovery.V8 microscope at the Institute of Earth Sciences, Heidelberg University, Germany. Results indicate excellent test preservation (see *SI Appendix, Section S4.2.1*).

Oxygen-isotope and Mg/Ca analyses

The oxygen-isotope composition of *O. umbonatus* for all samples investigated in this study was analyzed using a ThermoFinnigan MAT253 gas-source mass spectrometer equipped with a Gas Bench II at the Institute of Geosciences, Goethe-University Frankfurt, Germany. Values are reported relative to the Vienna Pee Dee Belemnite (VPDB). The external precision, determined from replicate measurements of an in-house carbonate standard (Carrara marble), is 0.06 ‰ (at 1σ level).

All samples of *O. umbonatus* for Mg/Ca analysis were cleaned following the cleaning protocol of ref. (65): First, the crushed test material was rinsed several times with MilliQ and methanol to remove clay minerals or any other fine-grained sedimentary material. Next, organic material was removed via oxidative cleaning using hydrogen peroxide buffered with sodium hydroxide. After oxidative cleaning, a reductive cleaning step (mixture of hydrazine, ammonium hydroxide and ammonium citrate) is often applied to remove coatings from test surfaces. However, we have omitted reductive cleaning because (i) it removes Mg from foraminiferal tests and therefore decreases their Mg/Ca ratios (65, 66), and (ii) after testing a pilot series of samples and their response to a cleaning procedure without reductive cleaning we found that coatings, if existent, did not affect measured Mg/Ca contents. Finally, a weak acid polish (0.001 M nitric acid) was used to remove contaminants that may have adsorbed on test-fragment surfaces during cleaning. Samples were subsequently dissolved in 0.075 M nitric acid for analysis. For quality control, we screened Al/Ca, Fe/Ca and Mn/Ca ratios during Mg/Ca analysis to check for Mg-bearing contaminant phases like clays or coatings not removed during cleaning that affect foraminiferal Mg/Ca ratios (65) (see *SI Appendix, Section S4.2.2*).

Samples for Mg/Ca analysis were measured using a Thermo Fischer Element High-Resolution Inductively Coupled Plasma Mass Spectrometer except for samples covering MIS 100, which were analyzed using a Perkin Elmer Optima 4300DV Inductively Coupled Plasma-Optical Emission Spectrometer; all Mg/Ca analyses were carried out at the University of Southampton National Oceanography Centre (UK). Exceptions are Mg/Ca ratios of core-top samples from MSM58, which were analyzed at the Institute of Earth Sciences, Heidelberg University, using an Agilent 720 Inductively Coupled Plasma-Optical Emission Spectrometer. Reported values were normalized relative to the ECRM 752-1 standard (Mg/Ca ratio of 3.762 mmol/mol (67)) to account for machine offsets. To ensure instrumental precision, an internal consistency standard was monitored. Replicate measurements yielded an uncertainty for Mg/Ca better than ± 1.31 %.

Palaeotemperature and sea-level reconstructions

In our paper, we differentiate between our best (sl-con$_{IGs}$) and most conservative (i.e., those calculations that minimize absolute sea levels and amplitudes of change) sea-level estimates. These were reconstructed as follows:

For our best estimates, Mg/Ca ratios were converted into BWTs using a species-specific equation for *O. umbonatus* derived from core-top calibrations (32) (BWT = {ln[(Mg/Ca)/1.008]}/0.114). This calibration is based on data obtained using a cleaning procedure that includes both oxidative and reductive cleaning of foraminiferal tests, whereas our samples required only oxidative cleaning (see above); thus, following refs. (65) and (68) measured Mg/Ca values were adjusted by reducing each value by 10 % before calculating BWTs. In addition, Mg/Ca values used for our BWT reconstruction were adjusted to past variations in Mg/Ca$_{sw}$. This was done by using equation (3) of ref. (32) and most recent estimates (36) of past Mg/Ca$_{sw}$ (minimum and maximum Mg/Ca$_{sw}$ values of 4.25 and 4.4 mol/mol, respectively). We note that such a correction relies on the assumption that the sensitivity of Mg incorporation in foraminiferal tests with respect to temperature remains the same under varying Mg/Ca$_{sw}$. For the MSM58 core-top samples as well as the "most recent samples" from Site U1313, a Mg/Ca$_{sw}$ correction was not applied as calcareous foraminiferal tests from these samples experienced present-day Mg/Ca$_{sw}$ conditions. The oxygen-isotope composition of seawater (relative to the Standard Mean Ocean Water [SMOW] standard) was then calculated (33, 69) using *O. umbonatus*-based δ^{18}O and BWT estimates ($\delta^{18}O_{sw,\,SMOW}$ = [(BWT – 16.9)/4.0] + $\delta^{18}O_b$ + 0.27). Finally, $\delta^{18}O_{sw}$ was converted to sea level (34) assuming that a 0.11 ‰ change in $\delta^{18}O_{sw}$ is equivalent to a 10 m change in sea level. Our most conservative sea-level estimates were calculated as described for our best estimates, but $\delta^{18}O_{sw}$

was converted to sea level (34) following the non-linear $\delta^{18}O_{sw}$-sea-level conversion of ref. (11) (brown line in Fig. 2) to minimize absolute sea levels.

Because our records come from the North Atlantic, application of the benthic $\delta^{18}O$-Mg/Ca approach to sea-level reconstruction requires an adjustment for changing deep-water masses with different local geochemical signatures that bathe the seafloor on glacial-interglacial timescales (37). Southern-sourced waters yield considerably lighter $\delta^{18}O_{sw}$ values compared to northern-sourced waters (38, 70). During glacials (interglacials) of our study interval, southern-sourced (northern-sourced) waters were dominating at Site U1313 (37), thus biasing $\delta^{18}O_{sw}$ towards lower (higher) values. To account for this water-mass difference in $\delta^{18}O_{sw}$, we applied a normalization factor to the foraminifer-derived $\delta^{18}O_{sw}$ values used for sea-level reconstruction. Following ref. (38), this normalization factor was calculated using a linear regression (BWT = 5 x $\delta^{18}O_{sw}$ + 2.6) between modern (70) North Atlantic Deep Water (2.6 °C and 0.1 ‰) and Antarctic Bottom Water (0 °C and -0.5 ‰) temperature and $\delta^{18}O_{sw}$ endmembers. This adjustment was carried out to calculate both our best estimates and our most conservative estimates. For the calculation of modern $\delta^{18}O_{sw}$ values from our "most recent" samples of Site U1313 and the core-top samples of MSM58, however, a water-mass adjustment is not required.

Tests presented in the supporting Supplementary Information indicate that our major conclusions are not highly sensitive to the assumptions that underpin our calculated best sea-level estimates and also emerge from our most conservative calculations (see, for example, *SI Appendix, Sections S4.2.5* and *S4.2.6*). All assumptions made in our paper to reconstruct sea level are summarized, critically assessed and evaluated in *SI Appendix* Section S4.2; in brief, this section contains additional information on the general quality of proxy data, the selection of calibrations to convert proxy data into sea level, and the potential influence of past Mg/Ca_{sw} and $\delta^{18}O_{sw}$ variability on our reconstruction.

Uncertainty band associated with sea-level reconstructions

The uncertainty associated with our sea-level reconstruction from Site U1313 (~2.75–2.4 Ma) was determined through Monte Carlo Simulations yielding 95 % non-parametric probability intervals. The Monte Carlo Simulation was carried out using the software R (version 3.4.2 (71)); input data for the simulation were the Mg/Ca and $\delta^{18}O$ values with their analytical errors and the BWT, $\delta^{18}O_{sw}$ and sea-level equations with their calibration errors (34). Thus, our approach relies on the following assumptions: The error in our sea-level record comes mainly from two sources, i.e., the uncertainties associated with $\delta^{18}O_{sw}$ estimation and sea-level calibration. The uncertainty in the $\delta^{18}O_{sw}$ reconstruction, in turn, mainly derives from errors in the $\delta^{18}O_{sw}$ calibration, the analytical precision of $\delta^{18}O$ measurements (± 0.06 ‰) and uncertainties in BWT estimates. The uncertainty in BWT estimates (± 1.11 °C) itself is based primarily on two factors: Analytical precision of Mg/Ca measurements (± 1.31 %) and error in the BWT calibration (32). Individual datapoints were randomly sampled 10,000 times within their proxy uncertainties. We then extracted 95 % confidence intervals for each time horizon based on the observed variability between the 2.5th and 97.5th percentile of the simulated data, roughly equivalent to 2σ (SD). Propagated uncertainties in individual sea-level estimates range from a minimum of ± 26.7 m to a maximum of ± 29.0 m, with a mean uncertainty of ± 28.0 m (note that main text refers to mean value). The calculated uncertainty is within the range of uncertainties typically associated with sea-level records reconstructed from paired benthic Mg/Ca and $\delta^{18}O$ records (± 20–30 m; see *SI Appendix, Section S3*).

Acknowledgements

We thank M. Cooper, J.O. Herrle, S. Hofmann, J.A. Milton and B. Schminke for laboratory assistance. Further we are grateful to M. Burchard for his support in statistical analyses. This research used samples provided by the Integrated Ocean Drilling Program. Funding for this study was provided by the German Research Foundation (DFG, grants FR2544/2 and FR2544/6 to O.F., JA2803/2-1 to K.A.J., and PR651/15 to J.P.), the European Union via a Marie Curie Fellowship to O.F. (Project PLIO-CLIMATE), and ECORD via a research grant to K.A.J. P.A.W. acknowledges funding from NERC (grant NE/D006465/1) and a Royal Society Wolfson Merit Award.

References

1. R. K. Pachauri et al., IPCC, *Climate Change 2014: Synthesis Report*, R. K. Pachauri et al., Eds. (IPCC, Geneva, Switzerland, 2014), p. 151.
2. R.S. Nerem *et al*., Climate-change-driven accelerated sea-level rise detected in the altimeter era. *Proc. Natl. Acad. Sci. U.S.A.* **115**, 2022–2025 (2018).
3. The IMBIE team, Mass balance of the Antarctic Ice Sheet from 1992 to 2017. *Nature* **558**, 219–222 (2018).
4. A. Shepherd, D. Wingham, Recent sea-level contributions of the Antarctic and Greenland Ice Sheets. *Science* **315**, 1529–1532 (2007).
5. J. Garbe, T. Albrecht, A. Levermann, J. F. Donges, R. Winkelmann, The hysteresis of the Antarctic Ice Sheet. *Nature* **585**, 538–544 (2020).
6. R. M. DeConto, D. Pollard, Contribution of Antarctica to past and future sea-level rise. *Nature* **531**, 591–597 (2016).
7. G. L. Foster. E. J. Rohling, Relationship between sea level and climate forcing by CO_2 on geological timescales. *Proc. Natl. Acad. Sci. U.S.A.* **110**, 1209–1214 (2013).
8. E. J. Rohling, I. D. Haigh, G. L. Foster, A. P. Roberts, K. M. Grant, A geological perspective on potential future sea-level rise. *Sci. Rep.* **3**, doi:10.1038/srep03461 (2013).
9. K. G. Miller *et al.*, Cenozoic sea-level and cryospheric evolution from deep-sea geochemical and continental margin records. *Science Advances* **6**, eaaz1346 (2020).
10. C. P. Cook *et al.* (2013), Dynamic behaviour of the East Antarctic ice sheet during Pliocene warmth. *Nat. Geosci.* **6**, 765–769.

11. E. Gasson, R. M. DeConto, D. Pollard, Modeling the oxygen isotope composition of the Antarctic ice sheet and its significance to Pliocene sea level. *Geology* **44**, 827–830 (2016).

12. M. O. Patterson *et al.,* Orbital forcing of the East Antarctic ice sheet during the Pliocene and Early Pleistocene. *Nat. Geosci.* **7,** 841–847 (2014).

13. O. Seki *et al.,* Alkenone and boron-based Pliocene pCO_2 records. *Earth Planet. Sci. Lett*. **292**, 201–211 (2010).

14. E. de la Vega, T. B. Chalk, P. A. Wilson, R. P. Bysani, G. L. Foster, Atmospheric CO_2 during the Mid-Piacenzian Warm Period and the M2 glaciation. *Sci. Rep.* **10**, 11002 (2020).

15. M. E. Raymo, J. X. Mitrovica, Collapse of polar ice sheets during the stage 11 interglacial. *Nature* **483**, 453–456 (2012).

16. P. J. van Hengstum, D. B. Scott, E. J. Javaux, Foraminifera in elevated Bermudian caves provide further evidence for 21 m eustatic sea level during Marine Isotope Stage 11. *Quat. Sci. Rev.* **28**, 1850–1860 (2009).

17. H. Elderfield *et al.,* Evolution of Ocean Temperature and Ice Volume Through the Mid-Pleistocene Climate Transition. *Science* **337**, 704–709 (2012).

18. S. Sosdian, Y. Rosenthal, Deep-sea temperature and ice volume changes across the Pliocene-Pleistocene climate transitions. *Science* **325,** 306–310 (2009).

19. T. Blackburn *et al.*, Ice retreat in Wilkes Basin of East Antarctica during a warm interglacial. *Nature* **583**, 554–559 (2020).

20. D. J. Wilson *et al.,* Ice loss from the East Antarctic Ice Sheet during late Pleistocene interglacials. *Nature* **561**, 383–386 (2018).

21. M. A. Martinez-Boti *et al.,* Plio-Pleistocene climate sensitivity evaluated using high-resolution CO_2 records. *Nature* **518**, 49–54 (2015).

22. C. T. Bolton *et al.,* Millennial-scale climate variability in the subpolar North Atlantic Ocean during the late Pliocene. *Paleoceanography* **25**, doi:4210.1029/2010PA001951 (2010).

23. D. C. Lang *et al.,* The transition on North America from the warm humid Pliocene to the glaciated Quaternary traced by eolian dust deposition at a benchmark North Atlantic Ocean drill site. *Quat. Sci. Rev.* **93**, 125–141 (2014).

24. G. Balco, C. W. Rovey, Absolute chronology for major Pleistocene advances of the Laurentide Ice Sheet. *Geology* **38,** 795–798 (2010).

25. L. E. Lisiecki, M. E. Raymo, A Pliocene-Pleistocene stack of 57 globally distributed benthic $\delta^{18}O$ records. *Paleoceanography* **20**, doi:1010.1029/2004PA001071 (2005).

26. R. M. DeConto *et al.* Thresholds for Cenozoic bipolar glaciation. *Nature* **455,** 652–656 (2008).

27. J. L. Bamber, R. L. Layberry, S. P. Gogineni, A new ice thickness and bed data set for the Greenland ice sheet. 1. Measurement, data reduction, and errors. *J. Geophys. Res.* **106,** 773–780 (2001).

28. M. J. Winnick, J. K. Caves, Oxygen isotope mass-balance constraints on Pliocene sea level and East Antarctic Ice Sheet stability. *Geology* **43**, 879–882 (2015).

29. P. Fretwell *et al.,* Bedmap2: improved ice bed, surface and thickness datasets for Antarctica. *The Cryosphere* **7**, 375–393 (2013).

30. Expedition 306 Scientists, in *Proc. IODP* **303/306**, J. E. T. Channel et al., Eds., doi:10.2204/iodp.proc.303306.112.2006 (2006).

31. C. H. Lear *et al.,* Neogene ice volume and ocean temperatures: Insights from infaunal foraminiferal Mg/Ca paleothermometry. *Paleoceanography* **30**, doi:10.1002/ 2015PA002833 (2015).

32. C. H. Lear, Y. Rosenthal, N. Slowey, Benthic foraminiferal Mg/Ca-paleothermometry: A revised core-top calibration. *Geochim. Cosmochim. Ac.* **66,** 3375–3387 (2002).

33. N. J. Shackleton, Attainment of isotopic equilibrium between ocean water and the benthonic foraminifera genus *Uvigerina*: isotopic changes in the ocean during the last glacial. *Cent. Natl. Rech. Sci. Colloq. Int.* **219**, 203–210 (1974).

34. R. G. Fairbanks, R. K. Matthews, The marine oxygen isotopic record in Pleistocene coral, Barbados, West Indies. *Quat. Res.* **10,** 181–196 (1978).

35. M. E. Raymo, R. Kozdon, D. Evans, L. E. Lisiecki, H. L. Ford, The accuracy of mid-Pliocene δ^{18}O-based ice volume and sea level reconstructions. *Earth-Science Reviews* **177**, 291–302 (2018).

36. D. Evans, C. Brierley, M.E. Raymo, J. Erez, W. Müller, Planktic foraminifera shell chemistry response to seawater chemistry: Pliocene–Pleistocene seawater Mg/Ca, temperature and sea level change. *Earth Planet. Sci. Lett.* **438,** 139–148 (2016).

37. D. C. Lang *et al.,* Incursions of southern-sourced water into the deep North Atlantic during late Pliocene glacial intensification. *Nat. Geosci.* **9**, 375–379 (2016).

38. G. S. Dwyer, M. A. Chandler, Mid-Pliocene sea level and continental ice volume based on coupled benthic Mg/Ca palaeotemperatures and oxygen isotopes. *Philos. T. Roy. Soc. A* **367**, 157–168 (2008).

39. D. W. Lea, P. A. Martin, D. K. Pak H. J. Spero, Reconstructing a 350 ky history of sea level using planktonic Mg/Ca and oxygen isotope records from a Cocos Ridge core. *Quat. Sci. Rev.* **21**, 283–293 (2002).

40. D. P. Schrag, G. Hampt, D. W. Murray, Pore fluid constraints on the temperature and oxygen isotopic composition of the glacial ocean. *Science* **272**, 1930–1932 (1996).

41. N. Lhomme, G. K. C. Clarke, Global budget of water isotopes inferred from polar ice sheets. *Geophys. Res. Lett.* **32**, doi:10.1029/2005gl023774 (2005).

42. C. L. Batchelor *et al.*, The configuration of Northern Hemisphere ice sheets through the Quaternary. *Nat. Commun.* **10**, doi:10.1038/s41467-41019-11601-41462 (2019).

43. I. Bailey *et al.*, Flux and provenance of ice-rafted debris in the earliest Pleistocene sub-polar North Atlantic Ocean comparable to the Last Glacial Maximum. *Earth Planet. Sci. Lett.* **341–344**, 222–233 (2012).

44. B. de Boer, L. J. Lourens, R. S. van de Wal, Persistent 400,000-year variability of Antarctic ice volume and the carbon cycle is revealed throughout the Plio-Pleistocene. *Nat. Comm.* **5**, doi: 10.1038/ncomms3999 (2014).

45. J. Brigham-Grette *et al.,* Pliocene Warmth, Polar Amplification, and Stepped Pleistocene Cooling Recorded in NE Arctic Russia. *Science* **340**, 1421–1427 (2013).

46. M. Melles *et al.,* 2.8 million years of Arctic climate change from Lake El'gygytgyn, NE Russia. *Science* **337**, 315–320 (2012).

47. E. J. Rohling *et al.,* Sea-level and deep-sea-temperature variability over the past 5.3 million years. *Nature* **508**, 477–482 (2014).

48. R. Bintanja, R. Van de Wal, North American ice-sheet dynamics and the onset of 100,000-year glacial cycles. *Nature* **454**, 869–872 (2008).

49. S. C. Woodard *et al.,* Antarctic role in Northern Hemisphere glaciation. *Science* **346**, 847–851 (2014).

50. Grant, G. R. *et al.,* The amplitude and origin of sea-level variability during the Pliocene epoch. *Nature*, doi:10.1038/s41586-41019-41619-z (2019).

51. P. U. Clark, D. Pollard, Origin of the Middle Pleistocene Transition by ice sheet erosion of regolith. *Paleoceanography* **13**, 1–9 (1998).

52. I. Bailey *et al.*, A low threshold for North Atlantic ice rafting from "low-slung slippery" late Pliocene ice sheets. *Paleoceanography* **25**, PA1212, doi:1210.1029/2009PA001736 (2010).

53. D. Pollard, R. M. DeConto, R. B. Alley, Potential Antarctic Ice Sheet retreat driven by hydrofracturing and ice cliff failure. *Earth Planet. Sci. Lett.* **412**, 112–121 (2015).

54. J. Laskar *et al.*, A long-term numerical solution for the insolation quantities of the Earth. *Astronomy and Astrophysics* **428**, 261–285 (2004).

55. H. D. Pritchard *et al.,* Antarctic ice-sheet loss driven by basal melting of ice shelves. *Nature* **484**, 502–505 (2012).

56. J. Weertman, Stability of the junction of an ice sheet and an ice shelf. *J. Glaciol.* **13**, 3–11 (1974).

57. I. Joughin, R. B. Alley, Stability of the West Antarctic ice sheet in a warming world. *Nat. Geosci.* **4**, 506–513 (2011).

58. R. McKay *et al.,* Antarctic and Southern Ocean influences on Late Pliocene global cooling. *Proc. Natl. Acad. Sci. U.S.A.* **109**, 6423–6428 (2012).

59. D. M. Sigman, M. P. Hain, G. H. Haug, The polar ocean and glacial cycles in atmospheric CO_2 concentration. *Nature* **466**, 47–55 (2010).

60. S. Passchier, East Antarctic Ice-Sheet dynamics between 5.2 and 0 Ma from a high-resolution terrigenous particle size record, ODP Site 1165, Prydz Bay-Cooperation Sea. *Short Research Paper 043*, doi:10.3133/of2007-1047.srp043 (2007).

61. M. Mudelsee, M. E. Raymo, Slow dynamics of the Northern Hemisphere Glaciation. *Paleoceanography* **20**, PA4022, doi:4010.1029/2005PA001153 (2005).

62. B. D. A. Naafs *et al.*, Strengthening of North American dust sources during the late Pliocene (2.7 Ma). *Earth Planet. Sci. Lett.* **317**, 8–19 (2012).

63. J. Repschläger, *et al.*, NASGAF: North Atlantic Subtropical Gyre and Azores Front Geometry, Cruise No. MSM58- September 10 - October 07, 2016 - Reykjavik (Island)-Ponta Delgada (Portugal), *Maria S. Merian Berichte* (2016).

64. S. Rathmann, H. Kuhnert, Carbonate ion effect on Mg/Ca, Sr/Ca and stable isotopes on the benthic foraminifera *Oridorsalis umbonatus* off Namibia. *Marine Micropaleontology* **66**, 120–133 (2008).

65. S. Barker, M. Greaves, H. Elderfield, A study of cleaning procedures used for foraminiferal Mg/Ca paleothermometry. *Geochem. Geophys. Geosys.* **4**, doi:10.1029/2003GC000559 (2003).

66. Y. Rosenthal *et al.,* Interlaboratory comparison study of Mg/Ca and Sr/Ca measurements in planktonic foraminifera for paleoceanographic research. *Geochem. Geophys. Geosys.* **5**, doi:10.1029/2003GC000650 (2004).

67. M. Greaves *et al.,* Interlaboratory comparison study of calibration standards for foraminiferal Mg/Ca thermometry. *Geochem. Geophys. Geosys* **9**, doi:08010.01029/02008GC001974 (2008).

68. H. L. Ford, S. M. Sosdian, Y. Rosenthal, M. E. Raymo, Gradual and abrupt changes during the Mid-Pleistocene Transition. *Quat. Sci. Rev.* **148**, 222–233, doi:10.1016/j.quascirev.2016.07.005 (2016).

69. G. Hut, Consultant's group meeting on stable isotope reference samples for geochemical and hydrological investigations. *Rep. to Dir. Gen. Int. At. Energy*, Vienna, 42 pp. (1987).

70. H. Craig, L. I. Gordon, in *Stable Isotopes in Oceanographic Studies and Paleotemperatures,* E. Tongiorgi, Ed. (Spoletto, 1965), pp. 9–130.

71. R Core Team. R: A language and environment for statistical computing. R Foundation for Statistical Computing, Vienna, Austria, http://www.R-project.org/ (2017).

Interglacial	Best sea-level estimate (sl-con$_{IGs}$)*	Most conservative sea-level estimate*
MIS G7	+ 35 m	+ 20 m
MIS G1	+ 18 m	+ 9 m
MIS 101	+ 44 m	+ 22 m

*Calculated as described in the *Methods*.

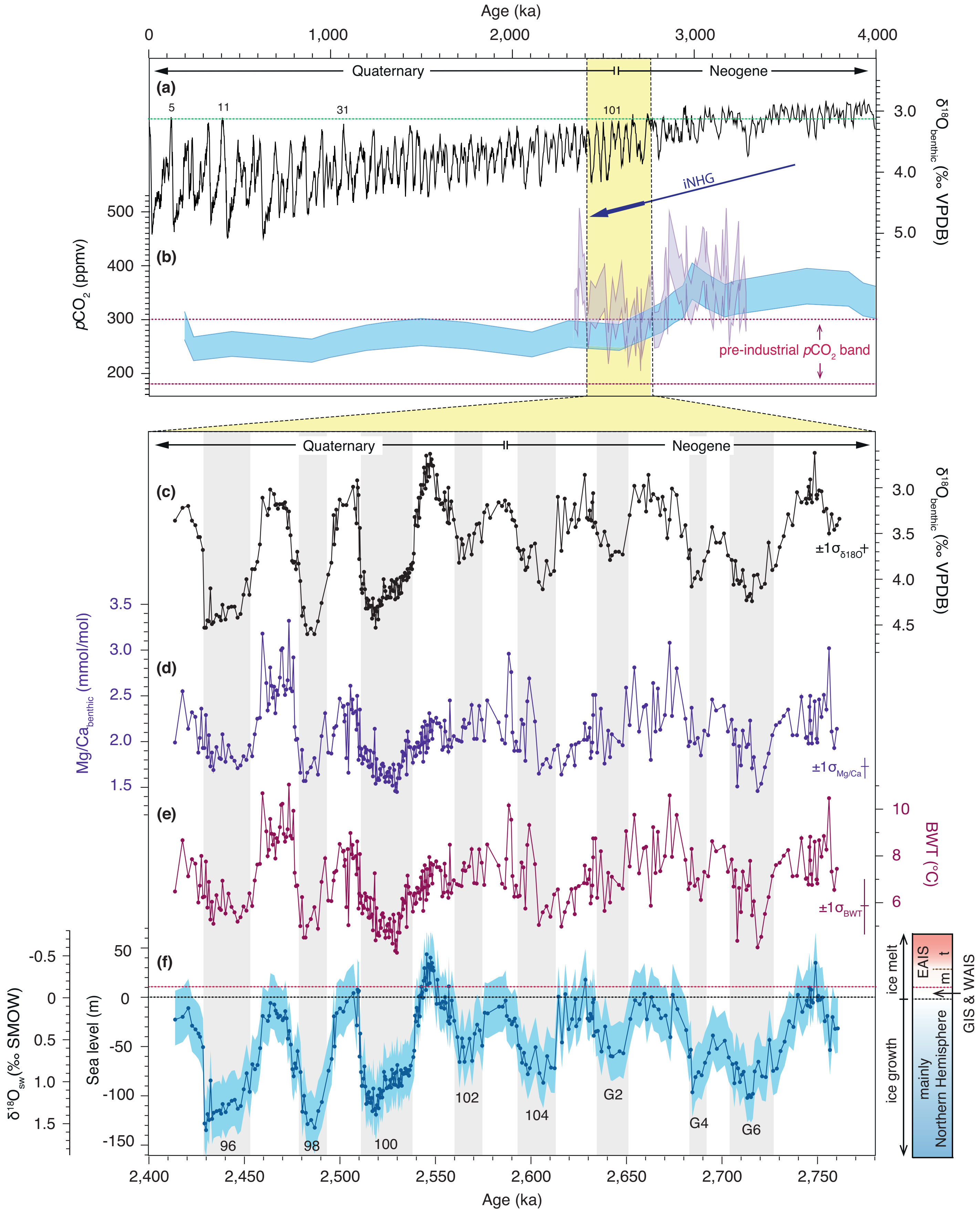

Age (ka)
0
1,000
2,000
3,000
4,000
Quaternary
Neogene
(a)
5
11
31
101
iNHG
δ18Obenthic (‰ VPDB)
3.0
4.0
5.0
500
400
300
200
pCO2 (ppmv)
(b)
pre-industrial pCO2 band
(c)
±1σδ18O
3.5
4.5
Mg/Cabenthic (mmol/mol)
(d)
2.5
2.0
1.5
±1σMg/Ca
(e)
BWT (°C)
10
8
6
±1σBWT
(f)
δ18Osw (‰ SMOW)
-0.5
0
0.5
1.0
1.5
Sea level (m)
50
-50
-100
-150
96
98
100
102
104
G2
G4
G6
ice melt
ice growth
EAIS
GIS & WAIS
mainly Northern Hemisphere
2,400
2,450
2,500
2,550
2,600
2,650
2,700
2,750

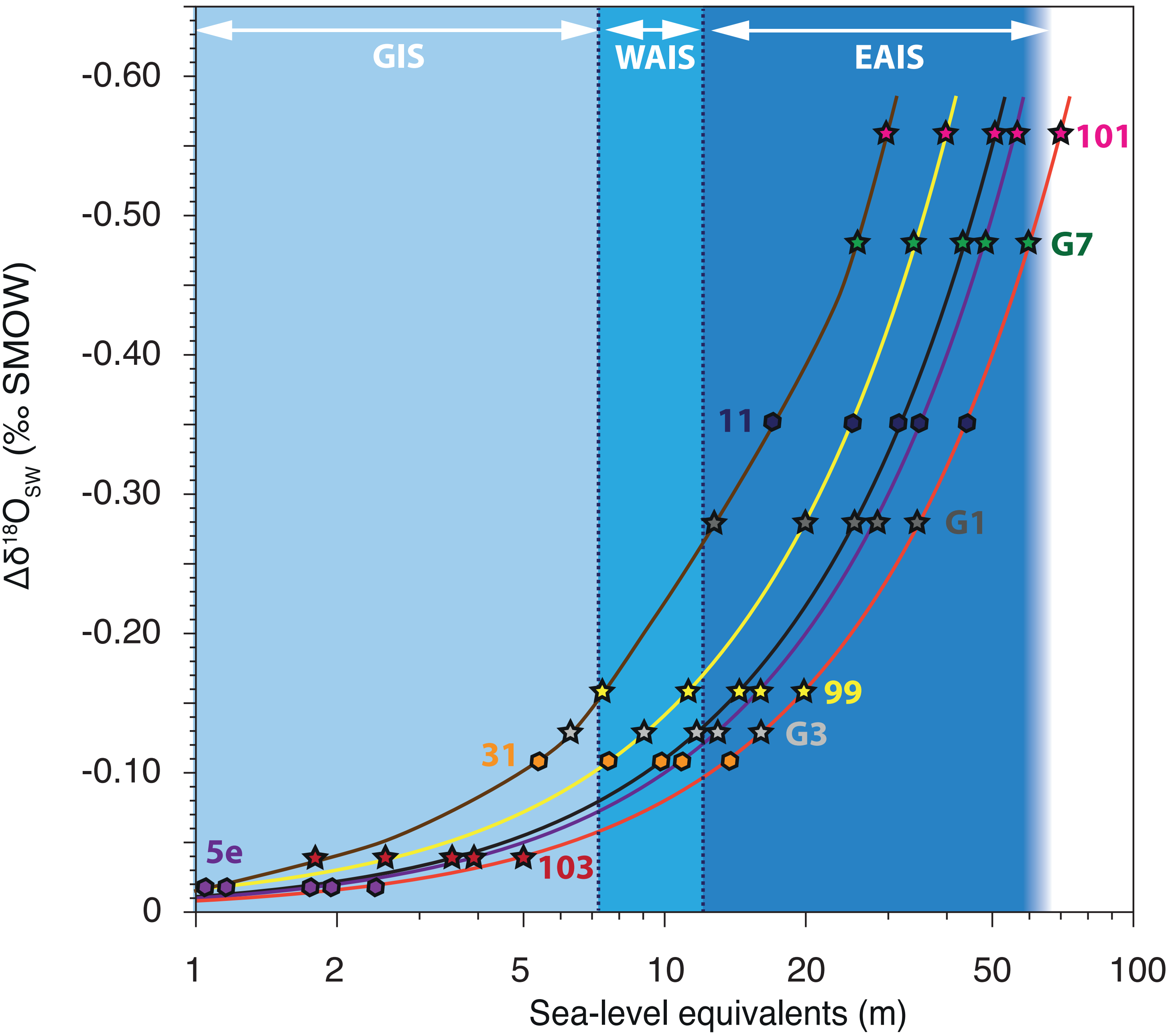

GIS
WAIS
EAIS
-0.60
-0.50
-0.40
-0.30
-0.20
-0.10
0
Δδ18OSW (‰ SMOW)
1
2
5
10
20
50
100
Sea-level equivalents (m)
101
G7
11
G1
99
G3
31
5e
103

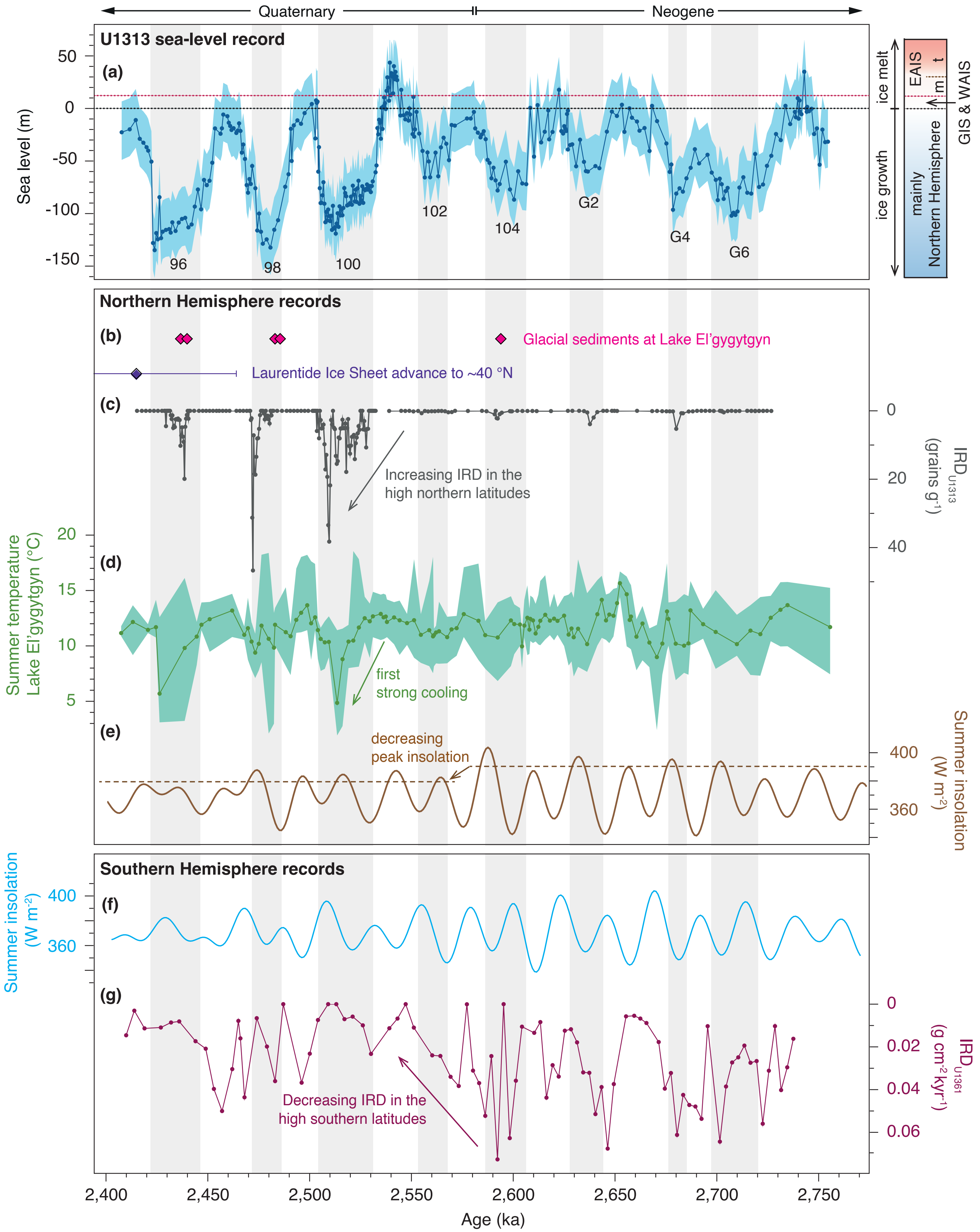
Quaternary
Neogene
U1313 sea-level record
(a)
Sea level (m)
50
0
-50
-100
-150
96
98
100
102
104
G2
G4
G6
ice melt
ice growth
EAIS
m
t
GIS & WAIS
mainly Northern Hemisphere
Northern Hemisphere records
(b)
Glacial sediments at Lake El'gygytgyn
Laurentide Ice Sheet advance to ~40 °N
(c)
Increasing IRD in the high northern latitudes
0
20
40
IRD U1313 (grains g-1)
(d)
Summer temperature Lake El'gygytgyn (°C)
20
15
10
5
first strong cooling
(e)
decreasing peak insolation
400
360
Summer insolation (W m-2)
Southern Hemisphere records
(f)
Summer insolation (W m-2)
400
360
(g)
Decreasing IRD in the high southern latitudes
0
0.02
0.04
0.06
IRD U1361 (g cm-2 kyr-1)
2,400
2,450
2,500
2,550
2,600
2,650
2,700
2,750
Age (ka)

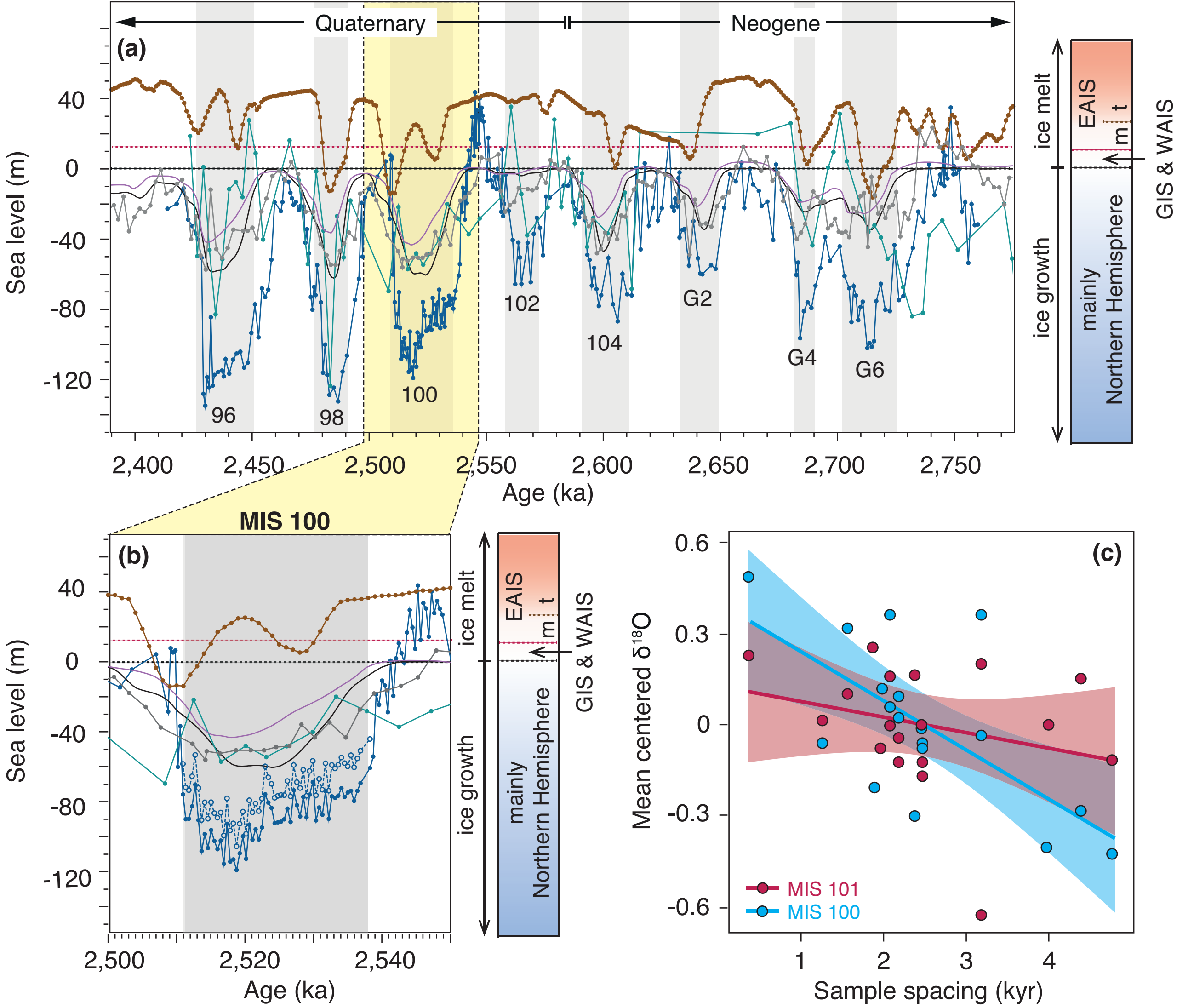

Quaternary
Neogene
(a)
Sea level (m)
40
0
-40
-80
-120
96
98
100
102
104
G2
G4
G6
2,400
2,450
2,500
2,550
2,600
2,650
2,700
2,750
Age (ka)
ice melt
ice growth
EAIS
m
t
GIS & WAIS
mainly
Northern Hemisphere
MIS 100
(b)
2,500
2,520
2,540
(c)
Mean centered δ¹⁸O
0.6
0.3
0
-0.3
-0.6
1
2
3
4
Sample spacing (kyr)
MIS 101
MIS 100